

See discussions, stats, and author profiles for this publication at: <https://www.researchgate.net/publication/225094494>

# Controllable Synthesis of Hollow Bipyramid $\beta$ -MnO<sub>2</sub> and Its High Electrochemical Performance for Lithium Storage

ARTICLE in ACS APPLIED MATERIALS & INTERFACES · JUNE 2012

Impact Factor: 6.72 · DOI: 10.1021/am300410z · Source: PubMed

CITATIONS

35

READS

11

6 AUTHORS, INCLUDING:



**Qingguo Shao**

National Institute for Materials Science

7 PUBLICATIONS 398 CITATIONS

SEE PROFILE



**Wu-Xing Zhang**

Huazhong University of Science and Technology

30 PUBLICATIONS 952 CITATIONS

SEE PROFILE



**Yunhui Huang**

Huazhong University of Science and Technology

239 PUBLICATIONS 6,446 CITATIONS

SEE PROFILE

# Controllable Synthesis of Hollow Bipyramid $\beta$ -MnO<sub>2</sub> and Its High Electrochemical Performance for Lithium Storage

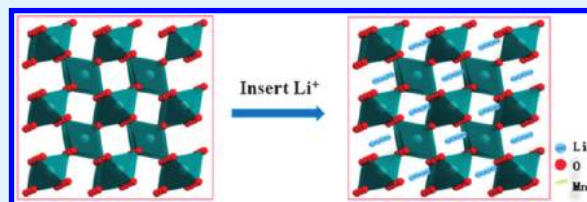
Wei-Min Chen,<sup>†,‡</sup> Long Qie,<sup>†</sup> Qing-Guo Shao,<sup>†</sup> Li-Xia Yuan,<sup>†</sup> Wu-Xing Zhang,<sup>†</sup> and Yun-Hui Huang<sup>\*,†</sup>

<sup>†</sup>State Key Laboratory of Material Processing and Die and Mold Technology, School of Materials Science and Engineering, Huazhong University of Science and Technology, Wuhan, Hubei 430074, China

<sup>‡</sup>Department of Chemistry and Pharmaceutical Engineering, Wuhan University of Technology Huaxia College, Wuhan, Hubei 430223, China

**ABSTRACT:** Three types of MnO<sub>2</sub> nanostructures, viz.,  $\alpha$ -MnO<sub>2</sub> nanotubes, hollow  $\beta$ -MnO<sub>2</sub> bipyramids, and solid  $\beta$ -MnO<sub>2</sub> bipyramids, have been synthesized via a simple template-free hydrothermal method. Cyclic voltammetry and galvanostatic charge/discharge measurements demonstrate that the hollow  $\beta$ -MnO<sub>2</sub> bipyramids exhibit the highest specific capacity and the best cyclability; the capacity retains 213 mAh g<sup>-1</sup> at a current density of 100 mA g<sup>-1</sup> after 150 cycles. XRD patterns of the lithiated  $\beta$ -MnO<sub>2</sub> electrodes clearly show the expansion of lattice volume caused by lithiation, but the structure keeps stable during lithium insertion/extraction process. We suggest that the excellent performance for  $\beta$ -MnO<sub>2</sub> can be attributed to its unique electrochemical reaction, compact tunnel-structure and hollow architecture. The hollow architecture can accommodate the volume change during charge/discharge process and improve effective diffusion paths for both lithium ions and electrons.

**KEYWORDS:** MnO<sub>2</sub>, nanotubes, bipyramids, lithium storage



## INTRODUCTION

In recent years, nanoscaled electrode materials have attracted great interest for lithium-ion batteries because they can effectively improve specific capacity and cycle life due to their high surface area and size effect.<sup>1–3</sup> Among the numerous nanostructures, one-dimensional (1D) hollow nanostructure like nanotube or hollow sphere is particularly attractive since it shows short diffusion path lengths for ions and electrons, which facilitates excellent electrochemical performance. Several methodologies such as sol–gel, hydrothermal route, template-assisted or template-free synthesis have been employed to fabricate various hollow nanostructures.<sup>4</sup> However, developing a facile, low-cost, and readily controllable method to attain 1D hollow nanostructure is still a challenge.

Various transition-metal oxides have been investigated as electrode materials for lithium storage, such as MnO<sub>2</sub>,<sup>5–7</sup> SnO<sub>2</sub>,<sup>8–10</sup> TiO<sub>2</sub>,<sup>11</sup> and MoO<sub>3</sub>.<sup>12,13</sup> Among them, MnO<sub>2</sub> has attracted tremendous research interest due to its low cost, high energy density and environmental friendliness.<sup>14</sup> Up to now, various polymorphs of MnO<sub>2</sub>, such as  $\alpha$ -,  $\beta$ -,  $\gamma$ -,  $\delta$ -, and  $\epsilon$ -types with different morphologies, have been reported.<sup>15–20</sup> Wang et al. reported that  $\beta$ -MnO<sub>2</sub> nanorods or  $\alpha$ -MnO<sub>2</sub> nanowires can be selectively prepared by simply changing the amount of ammonium sulfate.<sup>21</sup> Hill et al. synthesized all the  $\alpha$ -,  $\beta$ -, and  $\gamma$ -MnO<sub>2</sub>, and investigated their Li-ion insertion behaviors.<sup>22,23</sup> It is especially noted that the electrochemical performance of MnO<sub>2</sub> strongly depends on its crystal structure, morphology and particle size. The specific capacity of MnO<sub>2</sub> is generally limited by its poor electrode kinetics because only the molecules located within a very thin layer at outside surface

participate in the charge-storage process while the rest remain inactive. How to insert more lithium ions into the lattice of MnO<sub>2</sub> is crucial to achieve a high capacity. On the other hand, because MnO<sub>2</sub> is irreversibly transformed to lithium manganese oxide during charge/discharge process, the cycle performance of MnO<sub>2</sub> is usually poor.<sup>17</sup> Among the MnO<sub>2</sub> polymorphs, much attention has been paid to  $\beta$ -MnO<sub>2</sub> because of its high specific capacity,<sup>6,24</sup> although  $\beta$ -MnO<sub>2</sub> has the narrowest (1 × 1) tunnel among the tunnel-type manganese oxide family. Nevertheless, further improvement in cyclic stability and rate capability for  $\beta$ -MnO<sub>2</sub> is still necessary. Moreover, the mechanism for the electrochemical properties of  $\beta$ -MnO<sub>2</sub> is not very clear, which needs to be identified.<sup>25</sup>

In this work, we report a facile hydrothermal process to prepare three different  $\alpha$ -MnO<sub>2</sub> and  $\beta$ -MnO<sub>2</sub> nanostructures with controllable crystal structure and morphology. The formation of three types of MnO<sub>2</sub> (nanotube, hollow bipyramid, solid bipyramid) was achieved by simply varying hydrothermal reaction temperature without any template or surfactant. Electrochemical measurements show that the as-synthesized hollow  $\beta$ -MnO<sub>2</sub> bipyramids exhibit the best discharge performance. Structural change and electrochemical mechanism of  $\beta$ -MnO<sub>2</sub> during lithiation process have been carefully investigated.

**Received:** March 7, 2012

**Accepted:** June 1, 2012

**Published:** June 1, 2012



## EXPERIMENTAL SECTION

**Synthesis of MnO<sub>2</sub>.** All chemical reagents used were of analytical grade. To prepare nanostructured MnO<sub>2</sub>, we mixed 2.8 mmol of KMnO<sub>4</sub> and 1.5 mL HCl (36 wt %) in 40 mL of deionized water and magnetically stirred the mixture for about 30 min to form a precursor solution. The solution was then transferred into a Teflon-lined stainless steel autoclave (70 mL) and heated at 160–200 °C in an oven for 12 h. After the autoclave was cooled to room temperature, the solid precipitate was centrifuged and rinsed for several times with deionized water and absolute ethanol to remove impurities, and finally dried in a vacuum at 80 °C for 12 h.

**Characterization.** The phase and structure were examined by X-ray diffraction (XRD) on a X'Pert PRO diffractometer (PANalytical B.V., Holland) with high intensity Cu K $\alpha$  irradiation ( $\lambda = 1.5406$  Å). The operation voltage and current were 40 kV and 40 mA, respectively. The morphologies of the samples were characterized by field-emission scanning electron microscopy (FE-SEM, FEI, Sirion 200) and their elemental compositions were measured with an energy-dispersive X-ray spectrometer (EDX, Oxford Instrument) attached to the FE-SEM. High-resolution transmission electron microscopy (HRTEM) observations were carried out on a JEM-2100F microscope (JEOL). X-ray photoelectron spectroscopy (XPS) measurements were performed on a VG MultiLab 2000 system with a monochromatic Al K $\alpha$  X-ray source (ThermoVG Scientific). The specific Brunauer–Emmett–Teller (BET) surface area was determined by N<sub>2</sub> adsorption/desorption on a BelSorp-Mini instrument (Ankersmid Co. Ltd.).

**Electrochemical Measurement.** The working electrodes were prepared by mixing 70 wt % of the as-synthesized MnO<sub>2</sub>, 20 wt % acetylene black, and 10 wt % polyvinylidene difluoride (PVDF) to form a slurry with N-methylpyrrolidone (NMP) as solvent. Then the slurry was coated onto an aluminum foil substrate and dried in a vacuum oven for 12 h. The electrochemical test was performed with CR2032 coin-type cells assembled in glovebox under argon atmosphere. The commercial electrolyte was composed of 1 mol L<sup>-1</sup> LiPF<sub>6</sub> in a 1:1 solvent mixture of ethylene carbonate and diethyl carbonate (EC/DEC). The galvanostatic charge–discharge tests were carried out using the Land battery measurement system (Wuhan, China) with a cutoff voltage of 1.5–4.3 V vs Li/Li<sup>+</sup> at the controlled temperature of 25 °C. Cyclic voltammetry (CV) curves were recorded on a PARSTAT 2273 potentiostat at a scan rate of 0.2 mV s<sup>-1</sup>.

## RESULTS AND DISCUSSION

The phase and crystallinity of the resulting materials were tested by powder XRD. As shown in Figure 1, the product

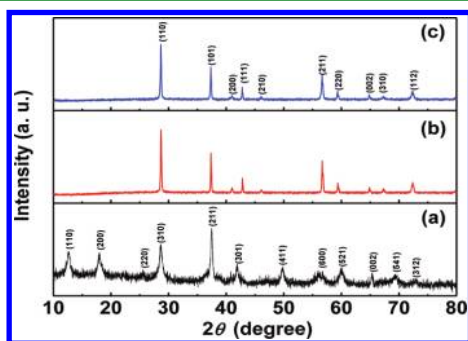


**Figure 1.** Power XRD patterns of the MnO<sub>2</sub> prepared at different temperatures: (a) 160 °C, (b) 180 °C, and (c) 200 °C.

prepared at 160 °C is identified to pure  $\alpha$ -MnO<sub>2</sub> (JCPDS No. 44–0141, tetragonal,  $I4/m$ ,  $a = b = 9.78$  Å,  $c = 2.86$  Å). When the temperature increases to 180 or 200 °C, the product is pure  $\beta$ -MnO<sub>2</sub> which diffraction peaks are narrow and strong (JCPDS No. 24–0735, tetragonal,  $P42/mnm$ ,  $a = b = 4.39$  Å,  $c = 2.87$  Å). For  $\alpha$ -MnO<sub>2</sub>, the broad diffraction peaks indicate that its

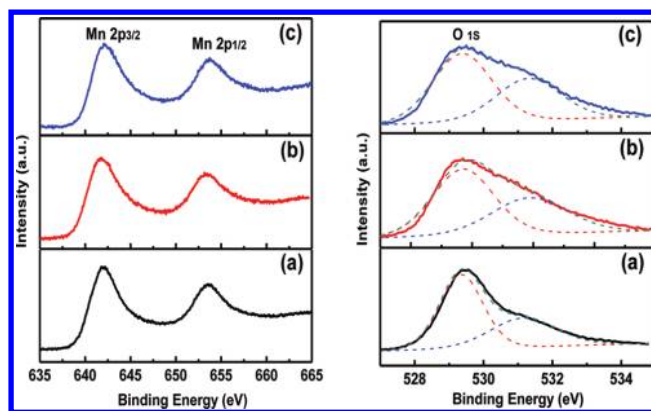


**Figure 2.** XPS of Mn 2p and O 1s for the MnO<sub>2</sub> samples prepared at different temperatures: (a) 160 °C, (b) 180 °C, and (c) 200 °C.

crystalline size is smaller and the crystallinity is worse as compared with  $\beta$ -MnO<sub>2</sub>. No impurity peaks are observed, indicating that high-purity  $\alpha$ -MnO<sub>2</sub> and  $\beta$ -MnO<sub>2</sub> can be attained by simply changing the hydrothermal reaction temperature.

Figure 2 shows XPS spectra of Mn 2p and O 1s for  $\alpha$ -MnO<sub>2</sub> and  $\beta$ -MnO<sub>2</sub>. The peaks of Mn 2p<sub>3/2</sub> and Mn 2p<sub>1/2</sub> are centered at 641.8 and 653.6 eV respectively, and their difference in binding energy is 11.8 eV. The data are in good agreement with those of MnO<sub>2</sub>.<sup>26</sup> The binding energy centered at 530 eV is attributed to O 1s, which can be deconvoluted into two peaks: one sharp peak at 529.5 eV and one broad peak at 531.4 eV. The peak at 529–530 eV responds to the lattice oxygen, while that at 531–532 eV can be assigned to defect oxygen or the surface oxygen ions.<sup>27</sup> It can be seen that there is no obvious difference in chemical composition on the surface between  $\alpha$ -MnO<sub>2</sub> and  $\beta$ -MnO<sub>2</sub>.

The morphologies and compositions of the MnO<sub>2</sub> samples prepared at different temperature were examined by FE-SEM and EDX. The sample obtained at 160 °C is tetragonal  $\alpha$ -MnO<sub>2</sub> that mainly consists of nanotubes (Figure 3a). The nanotubes show a square cross-section, with a diameter of 30–40 nm and length of several micrometers. The BET surface area of the nanotubes is 29 m<sup>2</sup> g<sup>-1</sup>, slightly larger than that of  $\alpha$ -MnO<sub>2</sub> nanotubes prepared at low temperature.<sup>19</sup> When the hydrothermal temperature increases to 180 °C,  $\beta$ -MnO<sub>2</sub> phase is formed. Most of the  $\beta$ -MnO<sub>2</sub> particles show a shape of hexagonal prism containing two pyramid ends with hollow interior, which can be regarded as hollow bipyramids. The unique morphology of  $\beta$ -MnO<sub>2</sub> should be formed because of some cracks or defections induced by the high hydrothermal temperature (Figure 3b). When the temperature increases to 200 °C, the product is still  $\beta$ -MnO<sub>2</sub>, but the morphology becomes solid bipyramid (Figure 3c). EDX analysis was employed to determine chemical composite of the  $\alpha$ -MnO<sub>2</sub> and  $\beta$ -MnO<sub>2</sub> samples (Figure 3d). The observed Si signal is due to the glass substrate. A small amount of K element is introduced into the sample; the atomic ratio of K to Mn in  $\alpha$ -MnO<sub>2</sub> is 9.3%. The incorporation of K is important for the formation of (2 × 2) + (1 × 1) tunnel structure in  $\alpha$ -MnO<sub>2</sub>. For  $\beta$ -MnO<sub>2</sub>, all of the peaks can be ascribed to Mn and O, which demonstrates that no K or any other elements are detected. The results are consistent with the XPS spectra for both  $\alpha$ - and  $\beta$ -MnO<sub>2</sub> samples.

Figure 4 shows SEM images of the MnO<sub>2</sub> samples prepared at different temperatures with various amounts of HCl. Figure

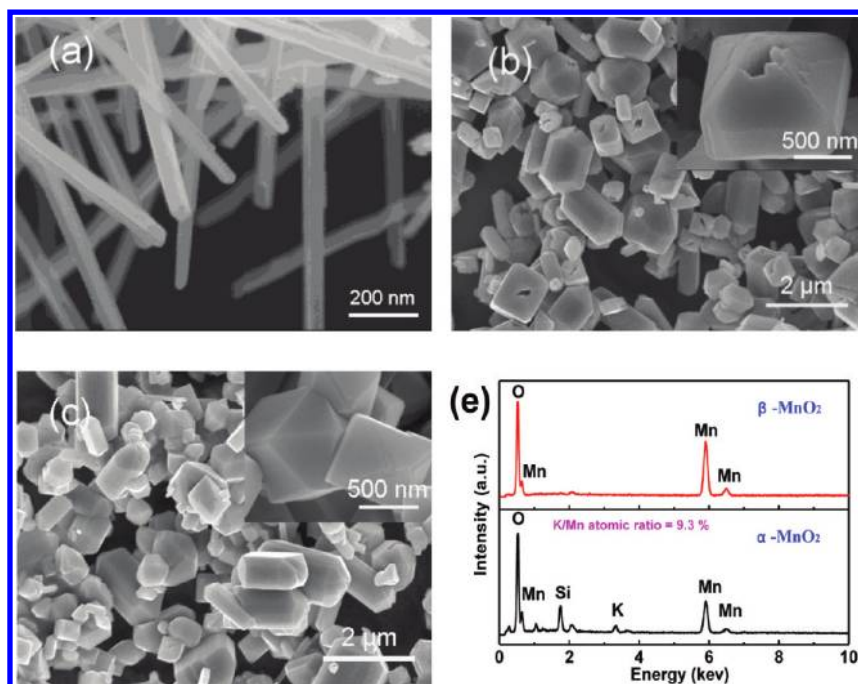


**Figure 3.** (a–c) FE-SEM images of the MnO<sub>2</sub> prepared at different temperatures: (a) 160 °C, (b) 180 °C, and (c) 200 °C; (d) EDX of the as-prepared  $\alpha$ -MnO<sub>2</sub> and  $\beta$ -MnO<sub>2</sub>.

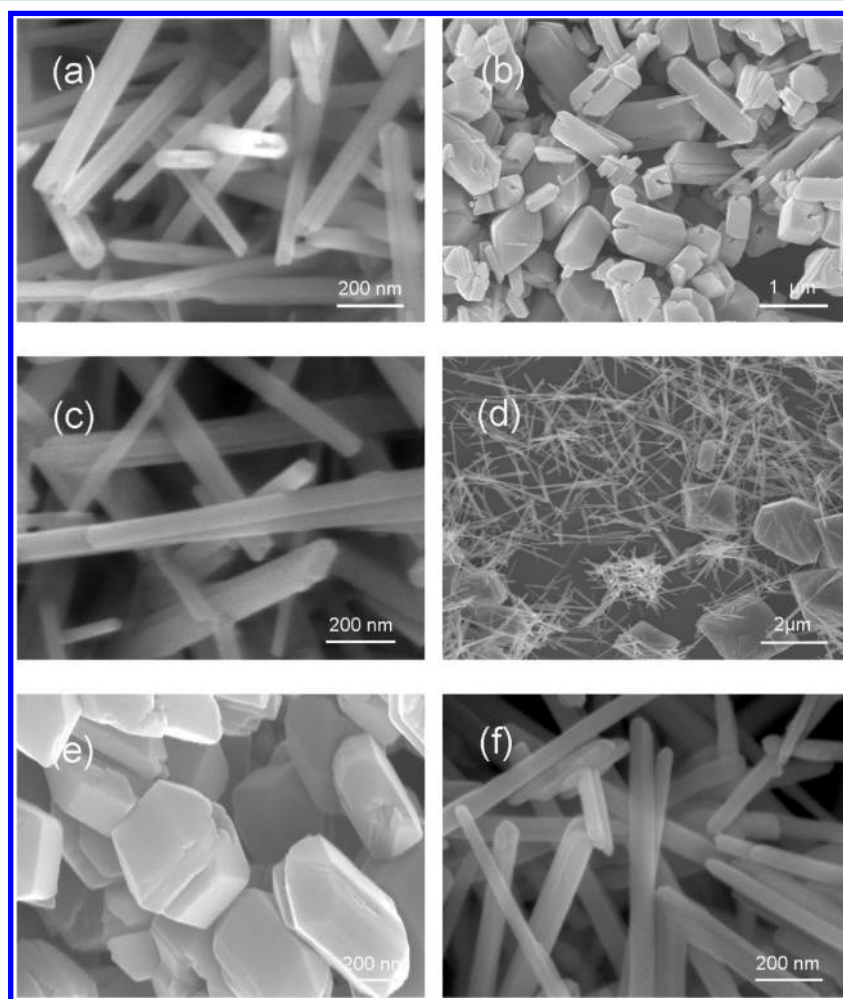


**Figure 4.** (a–f) FE-SEM images of the MnO<sub>2</sub> samples prepared at different conditions: (a) 1.0 mL HCl, 160 °C; (b) 2.0 mL HCl, 160 °C; (c) 1.0 mL HCl, 180 °C; (d) 1.3 mL HCl, 180 °C; (e) 2.0 mL HCl, 180 °C; (f) 1.0 mL HCl, 200 °C.



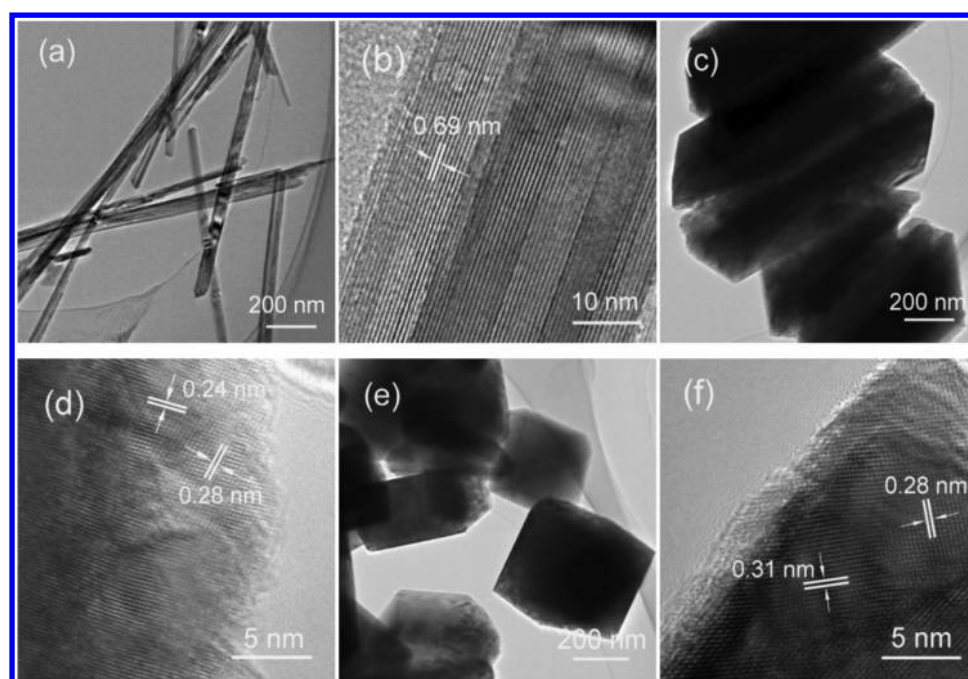


**Figure 5.** (a, c, e) TEM and (b, d, f) HRTEM images for the  $\text{MnO}_2$  samples prepared at different temperatures: (a, b) 160 °C, (c, d) 180 °C, and (e, f) 200 °C.

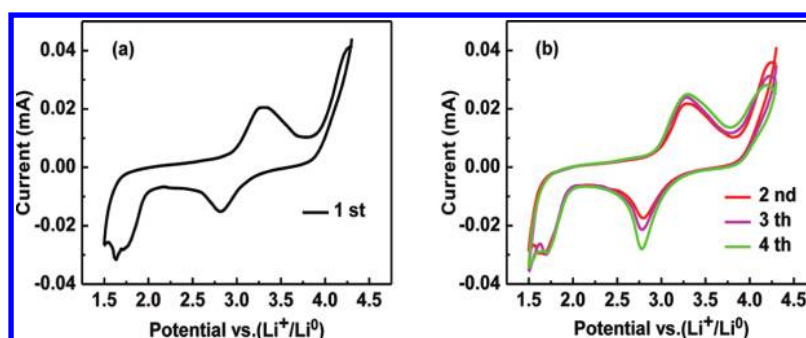


**Figure 6.** CV curves of the hollow  $\beta\text{-MnO}_2$  bipyramids at a scan rate of  $0.2 \text{ mV s}^{-1}$  in the voltage range from 1.5 to 4.3 V.

4a, c, and f reveals that 1D  $\text{MnO}_2$  nanotubes or nanorods are attained at 160, 180, and 200 °C with only adding 1.0 mL HCl. With increasing HCl concentration, the amount of 1D nanostructured  $\text{MnO}_2$  decreases while nanorod and bipyramid crystals are observed (Figure 4b, d). If the HCl concentration is high, all  $\text{MnO}_2$  crystals become bipyramids with uniform size and rough surface (Figure 4e). It can be seen that high HCl concentration and high reactant temperature favor the formation of  $\text{MnO}_2$  bipyramids. The rough surface should be due to the corrosion caused by the excess used acid. The pH is believed to have a large influence on the crystal growth and morphology of  $\text{MnO}_2$ .<sup>23</sup> At the same time, since  $\text{Cl}^-$  can react as a reducer with  $\text{MnO}_4^-$  to form  $\text{MnO}_2$ , it certainly affects the formation of  $\text{MnO}_2$  crystals. With changing the HCl concentration, the amount of  $\text{Cl}^-$  ions varies synchronously with that of  $\text{H}^+$  ions. We believe that  $\text{Cl}^-$  and  $\text{H}^+$  ions have cooperative effect on the growth of  $\text{MnO}_2$ .

Further information of microstructure for the  $\alpha\text{-MnO}_2$  and  $\beta\text{-MnO}_2$  was provided by TEM characterization. Figure 5a displays a typical TEM image of  $\alpha\text{-MnO}_2$  nanotubes with homogeneous hollow structure. HRTEM analysis (Figure 5b) shows a lattice spacing of 0.69 nm, which agrees well with (110) interplanar distance of  $\alpha\text{-MnO}_2$ . The HRTEM pattern

demonstrates that the nanotubes grow along [002] direction. TEM images c and e in Figure 5 indicate that the two types of  $\beta\text{-MnO}_2$  both have tetragonal bipyramid morphologies. It is notable that the  $\beta\text{-MnO}_2$  prepared at 180 °C clearly shows a hollow structure, whereas the  $\beta\text{-MnO}_2$  prepared at 200 °C consists of inner solid framework. These results are consistent with those observed by SEM. Images d and f in Figure 5 show the HRTEM images taken from the edge of the  $\beta\text{-MnO}_2$  bipyramids, which give more detailed structural information. The marked lattice fringes with the spacings of 0.24, 0.28, and 0.31 nm are ascribed to the interplanar spacings between (101), (001), and (110) planes, respectively, for the tetragonal  $\beta\text{-MnO}_2$ . All of the well-resolved lattice fringes further indicate the high crystallinity for the two types of  $\beta\text{-MnO}_2$  bipyramids.

In general,  $\text{MnO}_2$  can form several polymorphs since the  $\text{MnO}_6$  octahedral units are linked in different ways. Structurally,  $\alpha\text{-MnO}_2$  is constructed from the double chains of edge-sharing  $\text{MnO}_6$  octahedra that are linked at the corners to form  $(2 \times 2) + (1 \times 1)$  tunnel structure, while  $\beta\text{-MnO}_2$  shows 1D channel  $(1 \times 1)$  structure composed of individual chains of the  $\text{MnO}_6$  octahedral units. Synthesis conditions, such as starting reagents, concentration and pH value of the precursor solution, play important roles in determining the morphology and tunnel

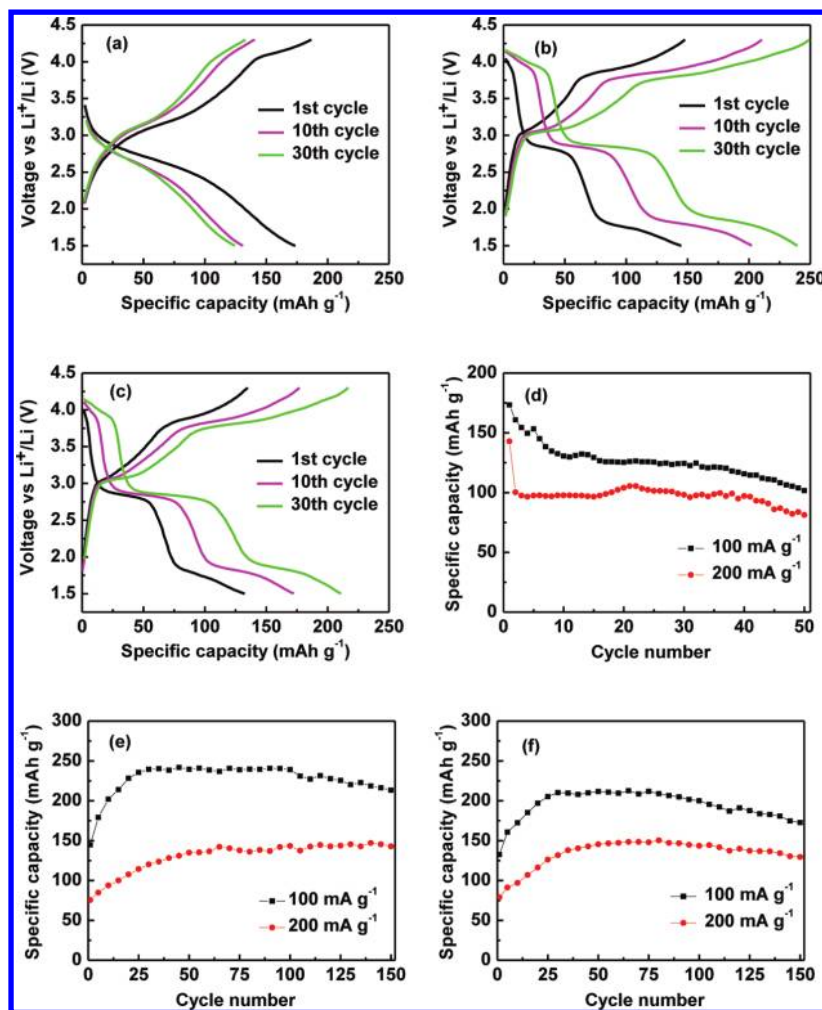


**Figure 7.** Galvanostatic charge and discharge curves and cycling performance for the  $\text{MnO}_2$  prepared at different temperatures: (a, d) 160 °C, (b, e) 180 °C, and (c, f) 200 °C.

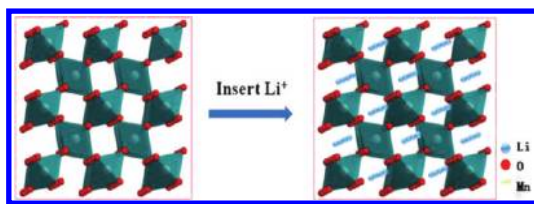


**Figure 8.** Schematic illustration for the insertion process of lithium ions into the crystal structure of  $\beta\text{-MnO}_2$ .

structure of  $\text{MnO}_2$ . A small amount of guest cations are usually required for the formation of tunnel structure.<sup>28</sup> The guest cations are commonly incorporated between the layers or inside the tunnels. Although the growing mechanisms for the three types of  $\text{MnO}_2$  nanostructures are difficult to be completely understood, we believe that  $\text{K}^+$  ions serve as the crucial guest cations. When the reaction takes place at 160 °C, a certain number of  $\text{K}^+$  ions direct the precursor to form  $(2 \times 2)$  tunnel structure of  $\alpha\text{-MnO}_2$ . XPS and EDX results have confirmed the existence of  $\text{K}^+$  ions in the  $\alpha\text{-MnO}_2$  phase. The formation of the nanotubes can be proposed as “etching” of the nanomaterials caused by HCl in the solution.<sup>19</sup> For the  $\text{MnO}_2$  crystals, since the end is metastable while the inner core has a higher surface energy, they are easily attacked by the acidic solution. The etching process is fast once the cracks or

defections are formed at the ends of  $\text{MnO}_2$  nanorods. As a result, the  $\text{MnO}_2$  nanorods are etched from outside to inside, and then hollow  $\text{MnO}_2$  nanotubes are formed so that the end metastable area is reduced and the lateral area with stable surface is enhanced. Since  $\alpha\text{-MnO}_2$  is a metastable phase, reaction at temperatures higher than 180 °C will promote the transformation of  $\alpha\text{-MnO}_2$  to more stable  $(1 \times 1)$  tunnel-structured  $\beta\text{-MnO}_2$  phase with compact framework. The  $(1 \times 1)$  tunnel of  $\beta\text{-MnO}_2$  is too small to accommodate  $\text{K}^+$  ions, which demonstrates that the guest ions cannot exist inside the tunnel. In fact, no  $\text{K}^+$  ions have been detected in  $\beta\text{-MnO}_2$  by both XPS and EDX, which confirms our suggested mechanism. After acidic “etching”, the tetragonal bipyramids uniformly become hollow. When the temperature is raised up to 200 °C, the high activity of  $\text{KMnO}_4$  and HCl leads to form large number of nuclei rapidly. As a consequence, solid tetragonal bipyramids with dense cores are formed via Ostwald ripening process. Therefore, it is feasible to control the morphology and structure of  $\text{MnO}_2$  by changing the reaction condition.

For insight into the electrochemical properties of the  $\alpha\text{-MnO}_2$  and  $\beta\text{-MnO}_2$ , CV and galvanostatic charge–discharge performance were tested. Figure 6 shows the CV curves of the hollow  $\beta\text{-MnO}_2$  bipyramids obtained at a scan rate of 0.2  $\text{mV s}^{-1}$  in the voltage range from 1.5 to 4.3 V. Clearly, the first scan cycle is slightly different from the other subsequent cycles. A

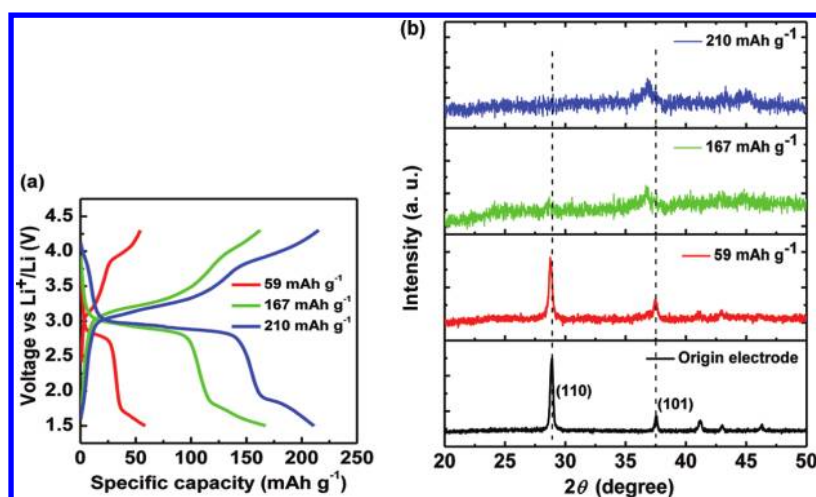


**Figure 9.** (a) Galvanostatic charge and discharge curves indexed to insertion of different amounts of lithium ions; (b) XRD patterns of the  $\beta$ -MnO<sub>2</sub> electrodes after insertion of different amounts of lithium ions.

broad peak in the first cathodic scan centers at about 1.6 V and it shifts to 1.75 V after the first cycle. With increasing scan cycle, the peak currents of the two redox peaks at 2.8 and 3.4 V clearly increase. The redox peaks should correspond to the absorption/desorption of lithium ions at the electrode surface and Li<sup>+</sup> insertion/extraction process in the lattice framework of MnO<sub>2</sub>, which agrees well with the previous reports.<sup>5,24</sup>

The first, 10th and 30th charge and discharge curves of the three types of MnO<sub>2</sub> between 1.5–4.3 V at a current density of 100 mA g<sup>-1</sup> are displayed in Figure 7. The charge/discharge curves for  $\alpha$ -MnO<sub>2</sub> and  $\beta$ -MnO<sub>2</sub> are obviously different. For  $\alpha$ -MnO<sub>2</sub> nanotubes, the specific charge and discharge capacities are 187 and 173 mAh g<sup>-1</sup>, respectively, for the first cycle (Figure 7a). However, the corresponding capacities drop to only 133 and 124 mA h g<sup>-1</sup> after 30 cycles, and no obvious potential plateau appears in all the cycles. In Figures 7b and c, the two types of  $\beta$ -MnO<sub>2</sub> bipyramids exhibit observable discharge plateaus at around 1.75 and 3.4 V, giving rise to higher discharge capacities than that of  $\alpha$ -MnO<sub>2</sub>. Moreover, the discharge capacity for  $\beta$ -MnO<sub>2</sub> increases gradually with cycling, which matches well with the CV curves. The hollow  $\beta$ -MnO<sub>2</sub> bipyramids show the best electrochemical performance with discharge capacity as high as 240 mA h g<sup>-1</sup> even after 30 cycles (Figure 7b). From both CV (Figure 6) and discharge curves (Figure 7b, c), it can be seen that  $\beta$ -MnO<sub>2</sub> shows a reaction at the potential of about 1.7 V, which gives additional capacity of about 70–90 mAh g<sup>-1</sup>. But for  $\alpha$ -MnO<sub>2</sub>, this reaction does not exist (Figure 7a). The electrochemical reaction at  $\sim$ 1.7 V can be ascribed to the process  $\text{MnO}_2 + 4\text{Li}^+ + 4\text{e}^- \rightarrow \text{Mn} + \text{Li}_2\text{O}$ . The unique electrochemical reaction for  $\beta$ -MnO<sub>2</sub> is the main reason for the better electrochemical performance than  $\alpha$ -MnO<sub>2</sub>.

Figure 7d–f presents long-term stability of the electrodes examined by galvanostatic charge/discharge cycling at current densities of 100 and 200 mA g<sup>-1</sup>. Apparently, bipyramid  $\beta$ -MnO<sub>2</sub> exhibits much better cyclability than that of nanotube  $\alpha$ -MnO<sub>2</sub>. For nanotube  $\alpha$ -MnO<sub>2</sub>, the discharge capacity after 50 cycles is only 102 mA h g<sup>-1</sup> at 100 mA g<sup>-1</sup> and 81 mA h g<sup>-1</sup> at 200 mA g<sup>-1</sup> (Figure 7d). For the two  $\beta$ -MnO<sub>2</sub> bipyramids, the specific capacity increases during the initial 40 cycles, and then remains stable. For the hollow  $\beta$ -MnO<sub>2</sub> bipyramids, the capacity and cyclability are superior to those for the solid  $\beta$ -MnO<sub>2</sub> bipyramids. The specific capacity retains 213 mA h g<sup>-1</sup>

at 100 mA g<sup>-1</sup> and 143 mA h g<sup>-1</sup> at 200 mA g<sup>-1</sup> after 150 cycles (Figure 7e), which is much higher than those reported previously.<sup>17,29</sup> Except for the unique electrochemical reaction mechanism, the compact (1  $\times$  1) tunnel-structure and hollow architecture also account for the high capacity and excellent cyclability for the hollow  $\beta$ -MnO<sub>2</sub> bipyramids.  $\beta$ -MnO<sub>2</sub> has a 1D structure containing (1  $\times$  1) tunnels with size of 0.189 nm.<sup>19</sup> Although the structure is not desirable for cation accommodation,<sup>30</sup> it is feasible for Li<sup>+</sup> insertion/extraction since the radius of Li<sup>+</sup> (0.068 nm) is much smaller than the (1  $\times$  1) tunnel size (Figure 8). Moreover, for  $\beta$ -MnO<sub>2</sub>, the compact (1  $\times$  1) structure can effectively relieve structural collapse and local volumetric variation during the charge/discharge process, which facilitates the enhancement in structural stability and cycling performance. However, for  $\alpha$ -MnO<sub>2</sub>, the two-tunnel structure is not stable and the incorporated K<sup>+</sup> ions may block the transportation of Li ions, resulting in low capacity and poor cyclability. As compared with the solid  $\beta$ -MnO<sub>2</sub> bipyramids, the hollow  $\beta$ -MnO<sub>2</sub> can provide more active sites for penetration of electrolyte and electrochemical reaction, and hence the kinetics of Li<sup>+</sup> and electron diffusion is highly improved. This effect has also been observed in other hollow or porous materials.<sup>24,26</sup>

To further understand the mechanism of lithium insertion in the  $\beta$ -MnO<sub>2</sub> bipyramids, we checked the XRD patterns of the  $\beta$ -MnO<sub>2</sub> electrodes after insertion of different amounts of lithium. As shown in Figure 9b, the diffraction peaks of the  $\beta$ -MnO<sub>2</sub> are similar to that of the origin electrode when the capacity reaches 59 mA h g<sup>-1</sup>. This indicates that insertion of a small amount of lithium does not change the structure of  $\beta$ -MnO<sub>2</sub>, and the framework of  $\beta$ -MnO<sub>2</sub> still remains high crystallinity. When the capacity reaches 167 mA h g<sup>-1</sup>, the discharge plateau at about 2.8 V broadens and the XRD peaks become weak, which means that insertion of large amount of lithium influences the crystallinity of  $\beta$ -MnO<sub>2</sub> phase. In addition, the 2 $\theta$  corresponding to (101) peak shifts to a lower angle with insertion of lithium, indicative of increase in lattice spacing and expansion in lattice volume. In other words, the increase in lattice spacing demonstrates that lithium ions are inserted into the lattice of  $\beta$ -MnO<sub>2</sub>. Further lithiation to 210 mA h g<sup>-1</sup>, the diffraction peaks become very weak and the peak at 2 $\theta$  = 28.6° almost disappears. This indicates that the crystallinity of  $\beta$ -MnO<sub>2</sub> degrades continuously and the lattice



volume further expands. It is thus concluded that insertion of Li ions leads to the increase in lattice spacing and cell volume for the nanocrystal  $\beta$ -MnO<sub>2</sub>. On the other hand, the crystallinity degradation to an amorphous-like structure for  $\beta$ -MnO<sub>2</sub> may lead to the enhancement of active points for the electrode materials, and hence improve the electrochemical performance. Similar phenomenon has been observed in other MnO<sub>2</sub>-based electrode materials.<sup>26</sup> The XRD patterns also show that there is no other phase formed during the charge/discharge cycling, which confirms that no irreversible structural change occurs when the oxygen atoms rearrange from tetragonal packing to cubic close-packing. Therefore, the excellent cyclic performance for  $\beta$ -MnO<sub>2</sub> can be ascribed to the reversible insertion/extraction reaction of lithium ions.

## CONCLUSIONS

A facile hydrothermal method has been developed to synthesize three types of MnO<sub>2</sub> nanostructures, viz.,  $\alpha$ -MnO<sub>2</sub> nanotubes, hollow  $\beta$ -MnO<sub>2</sub> bipyramids and solid  $\beta$ -MnO<sub>2</sub> bipyramids, by simply adjusting the reaction conditions. As the cathode material for lithium-ion batteries, hollow  $\beta$ -MnO<sub>2</sub> bipyramids exhibit superior electrochemical performance as compared to  $\alpha$ -MnO<sub>2</sub> nanotubes and solid  $\beta$ -MnO<sub>2</sub> bipyramids. The specific capacity of the hollow  $\beta$ -MnO<sub>2</sub> bipyramids reaches 213 and 143 mAh g<sup>-1</sup> at current density of 100 and 200 mA g<sup>-1</sup>, respectively, after 150 charge/discharge cycles. The high specific capacity and excellent cycling stability for the  $\beta$ -MnO<sub>2</sub> can be ascribed to its unique electrochemical reaction mechanism, compact (1 × 1) tunnel structure and hollow architecture. The tunnel structure and hollow architecture can effectively accommodate the volume change and improve diffusion paths for both lithium ions and electrons.

## AUTHOR INFORMATION

### Corresponding Author

\*E-mail: huangyh@mail.hust.edu.cn.

### Notes

The authors declare no competing financial interest.

## ACKNOWLEDGMENTS

This work was supported by the Natural Science Foundation of China (Grants 50825203 and 21175050), the 863 program from the MOST (Grants 2011AA11290 and 2011DFB70020), and the PCSIRT (Program for Changjiang Scholars and Innovative Research Team in University, IRT1014). In addition, the authors thank Analytical and Testing Center of Huazhong University of Science and Technology for XRD, SEM measurement.

## REFERENCES

- (1) Bruce, P. G.; Scrosati, B.; Tarascon, J. M. *Angew. Chem., Int. Ed.* **2008**, *47*, 2930–2946.
- (2) Cheng, F. Y.; Chen, J.; Gou, X. L.; Shen, P. W. *Adv. Mater.* **2005**, *17*, 2753–2756.
- (3) Reddy, A. L. M.; Shaijumon, M. M.; Gowda, S. R.; Ajayan, P. M. *Nano Lett.* **2009**, *9*, 1002–1006.
- (4) Chen, J. S.; Archer, L. A.; Lou, X. W. *J. Mater. Chem.* **2011**, *21*, 9912–9924.
- (5) Ouassim, G.; Jean-Louis, P.; Frederic, F. *ACS Appl. Mater. Interfaces* **2009**, *1*, 1130–1139.
- (6) Zeng, J. H.; Wang, Y. F.; Yang, Y.; Zhang, J. J. *Mater. Chem.* **2010**, *20*, 10915–10918.
- (7) Lei, Z.; Shi, F.; Lu, L. *ACS Appl. Mater. Interfaces* **2012**, *4*, 1058–1064.
- (8) Chen, J. S.; Cheah, Y. L.; Chen, Y. T.; Jayaprakash, N.; Madhavi, S.; Yang, Y. H.; Lou, X. W. *J. Phys. Chem. C* **2009**, *113*, 20504–20508.
- (9) Lou, X. W.; Chen, J. S.; Chen, P.; Archer, L. A. *Chem. Mater.* **2009**, *21*, 2868–2874.
- (10) Lou, X. W.; Li, C. M.; Archer, L. A. *Adv. Mater.* **2009**, *21*, 2536–2539.
- (11) Chen, J. S.; Tan, Y. L.; Li, C. M.; Cheah, Y. L.; Luan, D. Y.; Madhavi, S.; Boey, F. Y. C.; Archer, L. A.; Lou, X. W. *J. Am. Chem. Soc.* **2010**, *132*, 6124–6130.
- (12) Sun, Y. M.; Hu, X. L.; Luo, W.; Huang, Y. H. *ACS Nano* **2011**, *5*, 7100–7107.
- (13) Sun, Y. M.; Hu, X. L.; Yu, J. C.; Li, Q.; Luo, W.; Yuan, L. X.; Zhang, W. X.; Huang, Y. H. *Energy Environ. Sci.* **2011**, *4*, 2870–2877.
- (14) Toupin, M.; Brousse, T.; Belanger, D. *Chem. Mater.* **2004**, *16*, 3184–3190.
- (15) Wei, W.; Cui, X.; Chen, W.; Ivey, D. G. *J. Phys. Chem. C* **2008**, *112*, 15075–15083.
- (16) Wang, X.; Li, Y. D. *Chem. Commun.* **2002**, 764–765.
- (17) Lee, J.; Lee, J. M.; Yoon, S.; Kim, S. O.; Sohn, J. S.; Rhee, K. I.; Sohn, H. J. *J. Power Sources* **2008**, *183*, 325–329.
- (18) Zheng, Y. H.; Cheng, Y.; Bao, F.; Wang, Y. S.; Qin, Y. J. *Cryst. Growth* **2006**, *286*, 156–161.
- (19) Xiao, W.; Wang, D.; Lou, X. W. *J. Phys. Chem. C* **2010**, *114*, 1694–1700.
- (20) Zhang, Q.; Cheng, X. D.; Feng, X. H.; Qiu, G. H.; Tan, W. F.; Liu, F. J. *Mater. Chem.* **2011**, *21*, 5223–5225.
- (21) Wang, X.; Li, Y. D. *J. Am. Chem. Soc.* **2002**, *124*, 2880–2881.
- (22) Hill, L. I.; Verbaere, A.; Guyomard, D. *J. Power Sources* **2003**, *119*, 226–231.
- (23) Hill, L. I.; Portal, R.; Verbaere, A.; Guyomard, D. *Electrochem. Solid-State Lett.* **2001**, *4*, A180–A183.
- (24) Jiao, F.; Bruce, P. G. *Adv. Mater.* **2007**, *19*, 657–660.
- (25) Jung, W.; Il; Nagao, M.; Pitteloud, C.; Itoh, K.; Yamada, A.; Kanno, R. *J. Mater. Chem.* **2009**, *19*, 800–806.
- (26) Xia, H.; Lai, M. O.; Lu, L. *J. Mater. Chem.* **2010**, *20*, 6896–6902.
- (27) Liang, S. H.; Teng, F.; Bulgan, G.; Zong, R. L.; Zhu, Y. F. *J. Phys. Chem. C* **2008**, *112*, 5307–5315.
- (28) Shen, X. F.; Ding, Y. S.; Liu, J.; Cai, J.; Laubernds, K.; Zenger, R. P.; Vasiliev, A.; Aindow, M.; Suib, S. L. *Adv. Mater.* **2005**, *17*, 805–809.
- (29) Kijima, N.; Takahashi, Y.; Akimoto, J.; Awaka, J. *J. Solid State Chem.* **2005**, *178*, 2741–2750.
- (30) Devaraj, S.; Munichandraiah, N. *J. Phys. Chem. C* **2008**, *112*, 4406–4417.